Draft version September 15, 2021
Typeset using LaTeX **preprint2** style in AASTeX63

Determination of the Local Hubble Constant from Virgo Infall Using TRGB Distances

Yoo Jung Kim, Jisu Kang, Myung Gyoon Lee[1] and In Sung Jang[2]

[1] *Astronomy Program, Department of Physics and Astronomy, Seoul National University, 1 Gwanak-ro, Gwanak-gu, Seoul 08826, Republic of Korea*

[2] *Leibniz-Institut für Astrophysik Potsdam (AIP), An der Sternwarte 16, 14482, Potsdam, Germany*

(Accepted September 30, 2020)

Submitted to ApJ

ABSTRACT

An independent determination of H_0 is crucial given the growing tension between the Hubble constant, H_0, derived locally and that determined from the modeling of the cosmic microwave background (CMB) originating in the early universe. In this work, we present a new determination of H_0 using velocities and tip of the red giant branch (TRGB) distances to 33 galaxies located between the Local Group and the Virgo cluster. We use a model of the infall pattern of the local Hubble flow modified by the Virgo mass, which is given as a function of the cosmological constants (H_0, Ω_Λ), the radius of the zero-velocity surface R_0, and the intrinsic velocity dispersion, σ_v. Fitting velocities and TRGB distances of 33 galaxies to the model, we obtain $H_0 = 65.8 \pm 3.5(stat) \pm 2.4(sys)$ km s^{-1} Mpc^{-1} and $R_0 = 6.76 \pm 0.35$ Mpc. Our local H_0 is consistent with the global H_0 determined from CMB radiation, showing no tension. In addition, we present new TRGB distances to NGC 4437 and NGC 4592 which are located near the zero-velocity surface: D = 9.28 ± 0.39 Mpc and D = 9.07 ± 0.27 Mpc, respectively. Their spatial separation is $0.29^{+0.30}_{-0.03}$ Mpc, suggesting that they form a physical pair.

Keywords: Distance indicators (394), Stellar distance (1595), Galaxy stellar halos (598), Galaxy stellar content (621), Virgo Cluster (1772), Cosmology (343), Hubble constant (758), Cosmological parameters (339)

1. INTRODUCTION

The Hubble tension is the discrepancy in recent cosmology that the Hubble constant (H_0) determined locally is significantly larger than the global value determined by observation of cosmic microwave background radiation (CMB) by Planck Collaboration et al. (2020), $H_0 = 67.4 \pm 0.5$ km s^{-1} Mpc^{-1} (Riess (2019); Verde et al. (2019), and references therein). The tension has been emphasized since Riess et al. (2016) obtained $H_0 = 73.24 \pm 1.74$ km s^{-1} Mpc^{-1} based on an empirical Cepheid calibration of the absolute magnitudes of Type Ia supernovae in the more distant Hubble flow. As refinements to the techniques have been made, the measurement uncertainties have shrunk but the range of measured values have not, yielding $H_0 = 74.03 \pm 1.42$ km s^{-1} Mpc^{-1} recently (Riess et al. 2019). This is 4.4σ discrepant with the Planck result and can be interpreted as a significant disagreement between the measurements of H_0 from the early universe and from the late universe.

In order to understand the cause of this discrepancy, we must take a closer look at these different techniques. In particular, because the value of H_0 based on standard candles depends highly on the zero-point of the distance scale, another independent distance ladder aside from Cepheids is crucial. Thus, there has been much effort to measure H_0 independently using the tip of the red giant branch (TRGB) (Lee et al. 1993) method.

The TRGB is the truncation of the red giant branch (RGB) sequence that corresponds to the helium flash point in the evolutionary stages of low-mass stars. Thus, the TRGB appears as an edge of the RGB sequence in color magnitude diagrams (CMDs) and the luminosity of the TRGB varies only slightly with metallicity in I band. Therefore, the TRGB provides a robust standard

Corresponding author: Myung Gyoon Lee
yoojkim@astro.snu.ac.kr,mglee@astro.snu.ac.kr

candle (Lee et al. 1993; Jang & Lee 2017a,b; Lee & Jang 2018; Freedman et al. 2019, 2020).

Jang & Lee (2017b)(TIPSNU) obtained $H_0 = 71.17 \pm 1.66(stat) \pm 1.87(sys)$ km s^{-1} Mpc^{-1} by calibrating the luminosity of SNe Ia using TRGB distances to galaxies hosting SNe Ia. Their H_0 value weakened the Hubble tension as their value lies between those measured by the Cepheid-calibrated SNe Ia method and those measured from CMB analysis. Later, Freedman et al. (2019) (Carnegie-Chicago Hubble Program; CCHP) reduced the uncertainty using a larger sample, yielding $H_0 = 69.8 \pm 0.8(stat) \pm 1.7(sys)$ km s^{-1} Mpc^{-1} (revised to $69.6 \pm 0.8(stat) \pm 1.7(sys)$ in Freedman et al. (2020)). This value of the Hubble constant agrees at the 1.2σ level with that from the Planck Collaboration and at the 1.7σ level with that from the Cepheid distance scale.

To date, most measurements of the local H_0 use distant galaxies hosting supernovae in order to minimize the effects of peculiar velocities. However, galaxies located between the Local Group and the Virgo Cluster ($D = 16.5$ Mpc (Kashibadze et al. 2020)) can also be used to obtain H_0, if we simultaneously consider their peculiar motion and the Hubble flow. The local Hubble flow is modified by the gravity of the Virgo cluster, showing our infall pattern toward the center of the Virgo cluster. Lynden-Bell (1981) and Sandage (1986) suggested that accurate distances and velocities to outlying members of the Local Group can be used to determine the age of the universe and the mass of the Local Group, based on the timing argument (Kahn & Woltjer 1959). Their model was based on the Lemaître-Tolman-Bondi model, which describes the dynamics of a pressure-free spherically symmetric system of particles (Lemaître 1933; Tolman 1934; Bondi 1947). Peirani & de Freitas Pacheco (2006, 2008) modified the model by including the cosmological constant, Ω_Λ, and applied it to the Virgo infalling galaxies. Fitting 27 galaxies with Tully-Fisher distances to the theoretical velocity-distance relation, they obtained $H_0 = 71 \pm 9$ km s^{-1} Mpc^{-1}.

In this work, we use TRGB distances to galaxies between the Local Group and the Virgo cluster to determine H_0 with reduced uncertainty. The large uncertainty of H_0 in Peirani & de Freitas Pacheco (2008) is due to the large uncertainty of Tully-Fisher distance measurements, typically 15%. Given that uncertainties of TRGB distances are typically 5%, the use of TRGB distances to fit the velocity-distance relation is expected to yield a more precise determination of H_0.

Fortunately, TRGB distances to many galaxies in front of the Virgo cluster are available today. In particular, Karachentsev et al. (2014, 2018) observed 29 galaxies with Hubble Space Telescope (HST) and derived TRGB distances to these galaxies in order to investigate Virgo infall and estimate the dynamical mass within zero-velocity radius. Moreover, Tikhonov & Galazutdinova (2020) obtained TRGB distances to 18 additional galaxies from archival *HST* images and noted that six of them are projected onto the Virgo cluster.

Adding to these samples, we determine TRGB distances to two galaxies in the southern Virgo infall region using archival *HST* data: NGC 4437 and NGC 4592. Hyper Suprime-Cam (HSC) color images of these galaxies (Aihara et al. 2019) are shown in Figure 1. NGC 4437 (= NGC 4517) is an edge-on spiral galaxy and the brightest galaxy located beyond the Local Sheet in Karachentsev et al. (2014, 2018) samples. Its TRGB distance is measured to be 8.34 ± 0.83 Mpc by Karachentsev et al. (2014). NGC 4592 is a dwarf spiral galaxy located 1.8° away from NGC 4437 in the sky, but its TRGB distance has not been studied. The Tully-Fisher distance to NGC 4592 is 11.60 ± 2.30 Mpc (Sorce et al. 2014) and thus has not been included in the Local Volume (D < 11 Mpc) galaxies sample defined by Karachentsev et al. (2013).

This paper is structured as follows. In Section 2, we describe the *HST* data and the reduction process used for the TRGB measurement. In §3, we describe the methods and results of TRGB distance measurements. In §4, we illustrate on the Virgo infall fitting and determination of H_0. In §5.1, we discuss the physical separation between NGC 4437 and NGC 4592. In §5.2, we examine possible systematic uncertainties in our H_0 measurement. In §5.3, we compare our determination of H_0 with the ones from other studies. In §6, we summarize our main results.

2. DATA AND DATA REDUCTION

We use two fields of archival *HST* images to measure TRGB distances to NGC 4437 and NGC 4592, as shown by rectangles in Figure 1. The *HST* observations are summarized in Table 1. The NGC 4437 minor axis halo field was taken with *HST/ACS* F606W and F814W filters, and the NGC 4592 major axis halo field was observed with *HST/WFC3* F555W and F814W filters. Individual `.flc` (charge transfer efficiency corrected) frames of each filter were aligned using `TWEAKREG` then were combined using `ASTRODRIZZLE` (Gonzaga & et al. 2012).

For the detection and photometry of the point sources, we used the most recent version of `DOLPHOT` (Dolphin 2000). We used the `Fitsky` = 2 option for the local sky estimation, which is applicable for crowded field

Table 1. A Summary of *HST* Observations for NGC 4437 and NGC 4592 Fields

Field	R.A.	Decl.	Instrument	Exposure Time			Prop. ID
	(J2000)	(J2000)		F555W (V)	F606W (V)	F814W (I)	
NGC 4437	12:32:46.83	+00:05:01.1	ACS/WFC		1640s	2076s	12878
NGC 4592	12:39:10.54	–00:31:46.5	WFC3/UVIS	5530s		5674s	11360

photometry. We applied the selection criteria of point sources for both bands as follows: $-0.3 <$ `SHARP` < 0.3, `CROWD` < 0.25, `CHI` < 2.5, `ROUND` < 1, `flag` < 4, and `S/N` > 3. We used the Vega magnitude system following the `DOLPHOT` output parameters.

3. TRGB DISTANCES TO NGC 4437 AND NGC 4592

In this Section, we first describe our selection criteria for RGB star candidates. Then we show two different approaches to measure the tip: detection of edge response using Sobel filter (Lee et al. 1993) and maximum likelihood method (Méndez et al. 2002; Makarov et al. 2006). Next, we summarize our results and compare the TRGB detection methods. Lastly, we compare our TRGB distance to NGC 4437 with previous measurements.

3.1. *Selection of RGB Star Candidates*

We use spatial and color constraints to select RGB star candidates in the galaxies. We use stars in the outer region of the *HST* fields to avoid contamination from younger stellar populations and high stellar crowding as much as possible, as marked by blue solid lines in Figure 2. Since NGC 4437 is an edge-on disk galaxy, and the ACS field is shifted off the disk plane, halo stars can be effectively selected using spatial constraints. On the other hand, NGC 4592 was observed with WFC3, which has a smaller field of view, and the field lies at the center of the disk plane, so the outer regions of the NGC 4592 field may include a larger fraction of disk stars compared with NGC 4437.

CMDs of the selected stars are displayed in the left panels of Figure 3. The RGB sequence is seen clearly in the color range $1.1 < F606W - F814W < 1.7$ for NGC 4437 and $1.5 < F555W - F814W < 1.9$ for NGC 4592. For NGC 4592, vertical sequences of blue and red young stars are conspicuous around the color $F555W - F814W \sim 0$ and $F555W - F814W \sim 1.2$ (blue ones are blue supergiants and main-sequence stars, and red ones are red supergiants). Therefore, in order to minimize the contribution from young stars and other non-RGB sources, we selected RGB star candidates from the shaded regions. The selected stars are expected to

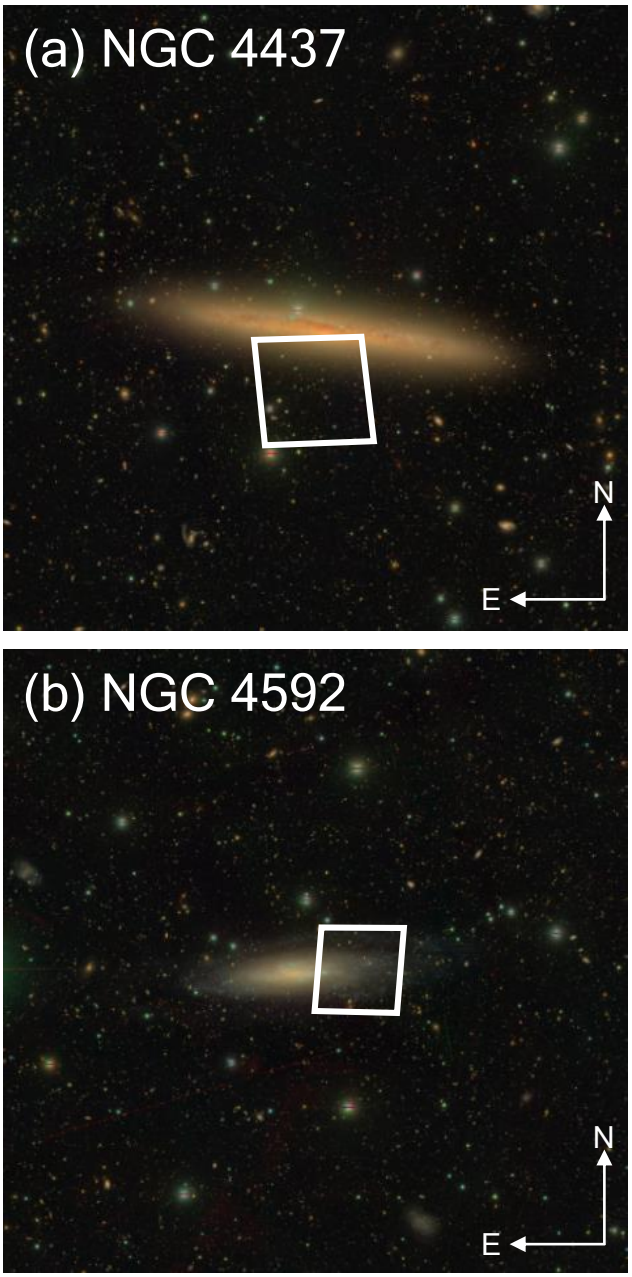

Figure 1. Hyper Suprime-Cam(HSC) g, r, i color images of (a) NGC 4437 (b) and NGC 4592 (Aihara et al. 2019). The field of view is $20' \times 20'$. *HST* fields taken with ACS (a) and WFC3 (b) are shown by white rectangles.

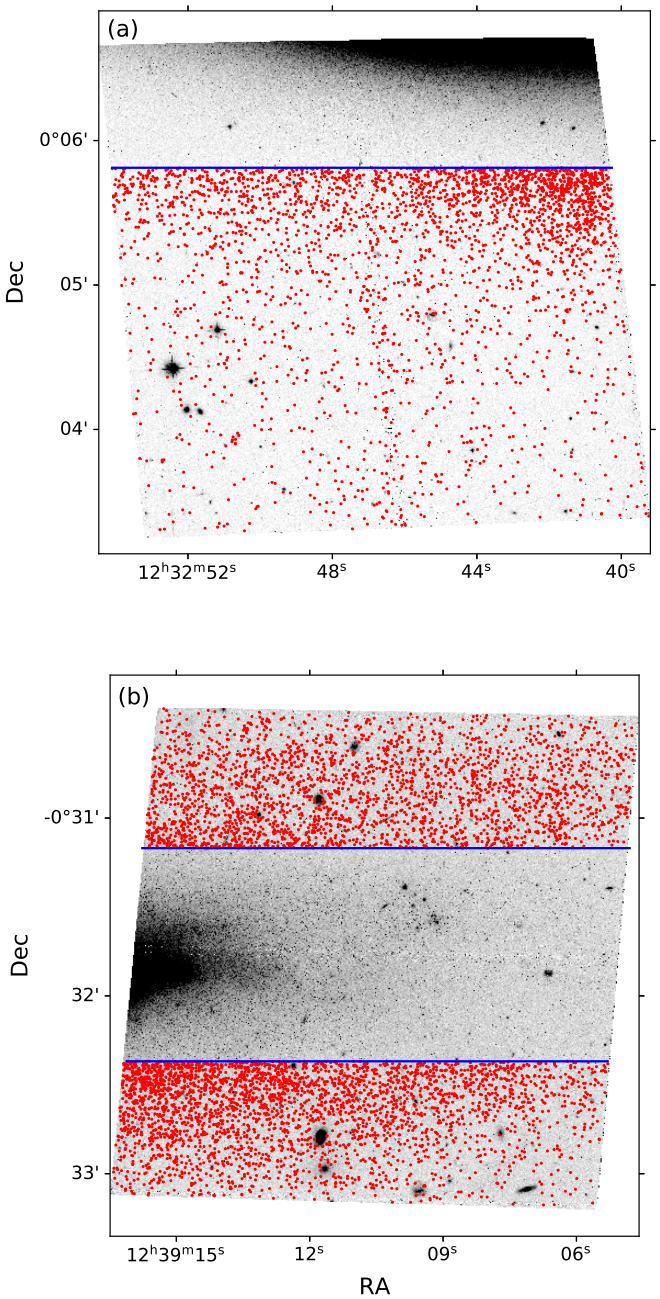

Figure 2. F814W *HST* images of (a) NGC 4437 and (b) NGC 4592. Blue solid lines denote boundaries of the spatial selection criteria. Red dots represent selected RGB star candidates from the shaded regions in Figure 3.

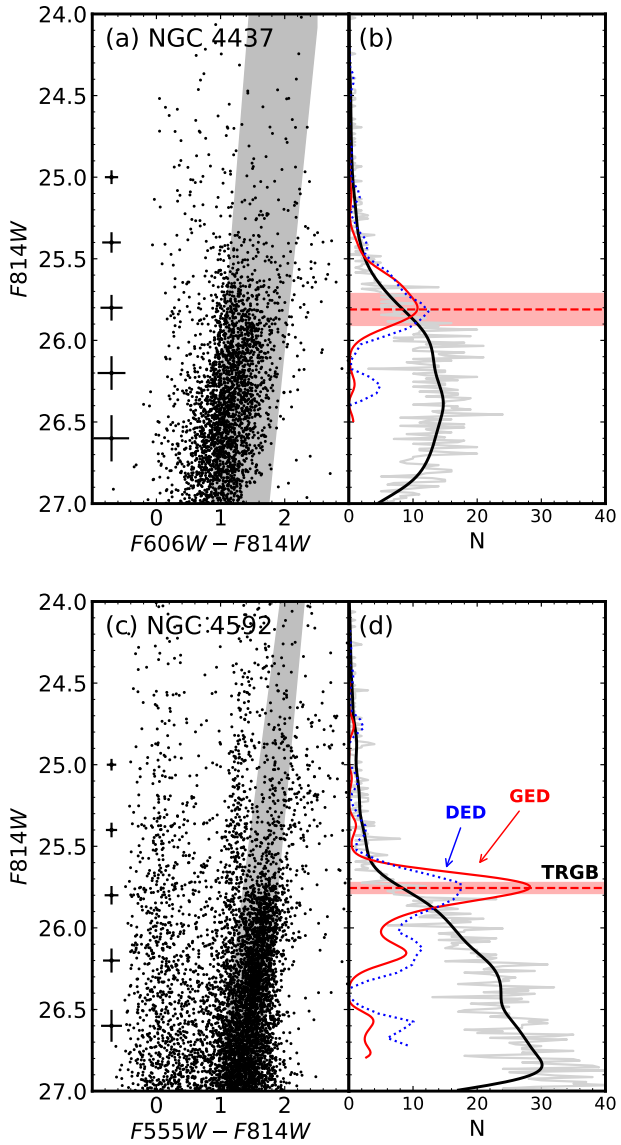

Figure 3. (Left) CMDs of spatially selected resolved stars in (a) NGC 4437 and (c) NGC 4592. Stars in the gray shaded region are selected as RGB star candidates. Mean photometric magnitude errors of RGB stars as a function of magnitude are shown as crosses on the left. (Right) LFs of selected RGB stars are shown as light gray lines and GLOESS-smoothed LFs are represented as black solid lines. Edge responses to the Sobel filter [−1, 0, +1] applied to GLOESS-smoothed LFs are shown as red solid lines (GLOESS edge detection; GED) and corresponding TRGBs are marked as red dashed lines. Edge responses of the direct edge detection (DED) method are plotted as blue dotted lines.

be dominated by old RGB stars and a few asymptotic giant branch (AGB) stars. The spatial locations of these stars are shown as red dots in Figure 2.

Finally, we conduct artificial star tests for RGB stars using DOLPHOT. We generate 50,000 artificial stars that satisfy the color and spatial constraints described above, in the magnitude range from $F814W = 24$ to 27 mag. Figure 4 shows the results of artificial star tests. The completeness (a number ratio of recovered stars to added

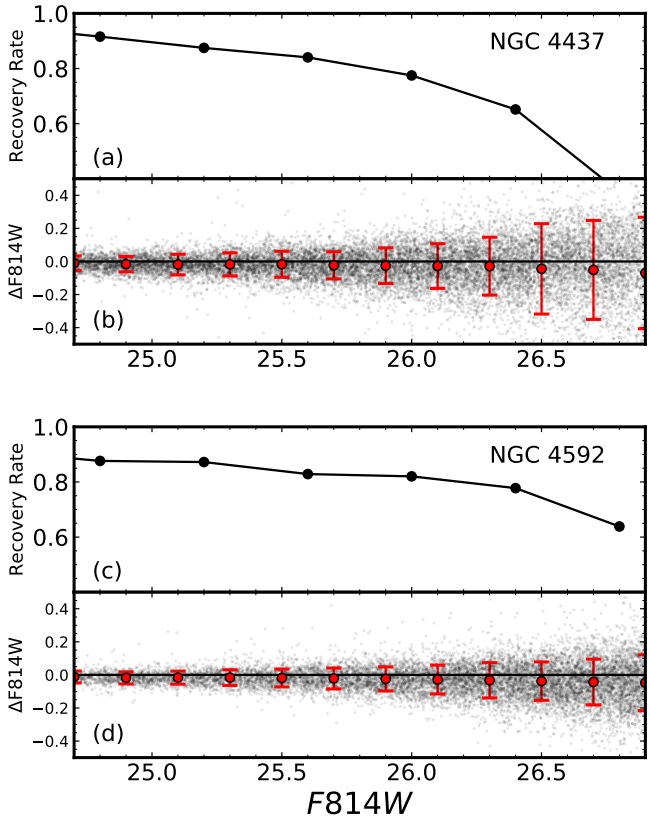

Figure 4. Panels (a) and (c): RGB star completeness derived from artificial star tests for NGC 4437 and NGC 4592, respectively. Panels (b) and (d): (Input mag – output mag) of artificial stars (gray dots). Red circles and error bars represent mean values and mean errors, respectively.

stars) as a function of input magnitude are shown in panels (a) and (c). The completeness reaches 50% level at about $F814W = 26.6$ mag for NGC 4437 and about $F814W = 27.0$ mag for NGC 4592. The input magnitude minus output magnitude of each star is shown in panels (b) and (d). The mean errors are smaller than 0.03 mag in the range of $F814W < 26$ mag.

3.2. *Edge Detection Method*

The basic concept of the edge detection method is an identification of the peak of the edge response, which is calculated by convolving the luminosity function (LF) of RGB stars with a Sobel kernel (Lee et al. 1993). There have been a number of refinements and variations since then (see Hatt et al. (2017) and Jang et al. (2018) for a comparison of recent methods). We use two of the recent methods in this study: (1) edge detection for smoothed LFs (Hatt et al. 2017) and (2) the direct edge detection method (Jang & Lee 2017b).

In Hatt et al. (2017), a finely binned (0.01 mag) LF of selected RGB candidates is smoothed using a Gaussian-windowed, locally weighted scatterplot smoothing (GLOESS), with the characteristic width of Gaussian weighting, σ_s. Then the Sobel kernel [–1, 0, +1] is applied to the smoothed LF, and the magnitude of maximum edge response corresponds to the TRGB. This smoothing technique is introduced in order to suppress false edges (Hatt et al. 2017). To find the optimal smoothing scale (σ_s) that minimizes the sum of systematic and random error, TRGB detection by the artificial star luminosity function (ASLF) was conducted (see Hatt et al. (2017) for details). We followed the same method and found optimal σ_s to be 0.10 mag and 0.08 mag for NGC 4437 and NGC 4592, respectively.

Figure 3 shows finely binned LFs (light gray lines), smoothed LFs (black solid lines), and edge responses (red solid lines) for these two galaxies. The maximum edge response is seen at $F814W_{\rm TRGB} \approx 25.8$ mag for both galaxies. For NGC 4437, the systematic error (input TRGB – output TRGB) obtained from the ASLF test is $\Delta\mu = 0.076$ mag and the random error is $\sigma = 0.055$ mag. Similarly, for NGC 4592, $\Delta\mu = 0.011$ mag and $\sigma = 0.020$ mag. Moreover, artificial star tests show that there are slight systematic magnitude offsets (input mag – output mag) at the TRGB magnitude: $\Delta F814W = -0.025$ mag for NGC 4437 and $\Delta F814W = -0.024$ mag for NGC 4592. These magnitude offsets are combined into systematic errors. Considering the uncertainties mentioned above, the TRGB magnitude of NGC 4437 is derived to be $F814W_{\rm TRGB} = 25.811 \pm 0.080$ (*sys*) $\pm$ 0.055 (*stat*) mag and that of NGC 4592 is $F814W_{\rm TRGB} = 25.756 \pm 0.026$ (*sys*) $\pm$ 0.020 (*stat*) mag. These results are summarized in Table 2.

Next, we try the direct edge detection method described in Jang & Lee (2017b). We apply a Sobel filter $[-1, -2, -1, 0, +1, +2, +1]$ directly to the LFs derived with a 0.05 mag bin. The edge response thus derived is shown as dotted blue lines in Figure 3. The maximum edge responses are seen at magnitudes similar to those from the GLOESS method. The uncertainty of the TRGB magnitude is obtained by bootstrap resampling RGB stars 10,000 times. Combining these errors with the systematic magnitude offsets given above, we derive $F814W_{\rm TRGB} = 5.829 \pm 0.049$ mag for NGC 4437 and $F814W_{\rm TRGB} = 25.763 \pm 0.050$ mag for NGC 4592, which are in excellent agreement with those of the GLOESS method.

We use the recent TRGB calibration of Jang et al. (2020) to obtain distances. Jang et al. (2020) used the megamaser-based distance to NGC 4258 (Reid

et al. 2019) as an anchor and obtained $M_{F814W}^{TRGB} = -4.050 \pm 0.028(stat) \pm 0.048(sys)$ in the ACS magnitude. This is applicable to the blue TRGB ($(F606W - F814W)_0 < 1.5$ or $(F555W - F814W)_0 < 2.1$), where I-band TRGB remains approximately constant with color. Mean TRGB colors of both NGC 4437 ($(F606W - F814W)_{0,\mathrm{TRGB}} = 1.20 \pm 0.10$) and NGC 4592 ($(F555W - F814W)_{0,\mathrm{TRGB}} = 1.65 \pm 0.06$) satisfy these criteria. Since the calibration is obtained in $F814W_{\mathrm{ACS}}$ magnitude system, we convert $F814W_{\mathrm{WFC3}}$ magnitude to $F814W_{\mathrm{ACS}}$ magnitude for NGC 4592 using the empirical transformation derived by Jang & Lee (2015). Here, we correct the apparent TRGB magnitudes for the foreground extinction: $A_{\mathrm{F606W(ACS)}} = 0.059$ and $A_{\mathrm{F814W(ACS)}} = 0.036$ for NGC 4437 and $A_{\mathrm{F555W(WFC3)}} = 0.055$ and $A_{\mathrm{F814W(WFC3)}} = 0.034$ for NGC 4592 (Schlegel et al. 1998; Schlafly & Finkbeiner 2011). Then the resulting distances for the GLOESS method are 9.22 ± 0.23 ($stat$) ± 0.41 (sys) Mpc for NGC 4437 and 9.03 ± 0.08 ($stat$) ± 0.25 (sys) Mpc for NGC 4592. For direct edge detection method, the resulting distances are 9.30 ± 0.18 ($stat$) ± 0.26 (sys) Mpc for NGC 4437 and 9.06 ± 0.18 ($stat$) ± 0.25 (sys) Mpc for NGC 4592. These results are summarized in Table 2. In Table 2, we also show the distances calibrated by Freedman et al. (2020), which used the geometric distance to the Large Magellanic Cloud as an anchor to TRGB ($M_{F814W}^{TRGB} = -4.054 \pm 0.022(stat) \pm 0.039(sys)$). It is noted that two calibrations agree well within 1%.

3.3. *Maximum Likelihood TRGB Detection Method*

We use the maximum likelihood TRGB detection method introduced by Méndez et al. (2002) and Makarov et al. (2006). This method fits an observed LF to a model with four free parameters (TRGB magnitude, RGB slope a, AGB slope c, and discontinuity b):

$$\psi = \begin{cases} 10^{a(m-m_{TRGB})+b}, & m - m_{TRGB} \geq 0 \\ 10^{c(m-m_{TRGB})}, & m - m_{TRGB} < 0. \end{cases} \quad (1)$$

We obtain a smoothed model by convolving the above model with photometric uncertainty and completeness from artificial star tests and use it for fitting. Sobel edge detection results derived above are used as initial guesses.

Figure 5 shows the results of the maximum likelihood optimization. Standard errors of the parameters are calculated by the square root of the inverse Hessian matrix. For NGC 4592, the slopes on both sides ($a = 0.50 \pm 0.06$, $c = 0.78 \pm 0.20$) are well-defined and the discontinuity is clear ($b = 0.47 \pm 0.09$). In contrast, for NGC 4437, the AGB slope ($c = 1.49 \pm 0.22$) is much larger and the discontinuity ($b = 0.20 \pm 0.13$) is smaller compared to those of NGC 4592, showing a more ambiguous tip. Combining the fitting errors with the systematic magnitude offsets given above, we derive the TRGB magnitude to be $F814W_{\mathrm{TRGB}} = 25.824 \pm 0.072$ mag for NGC 4437 and $F814W_{\mathrm{TRGB}} = 25.765 \pm 0.034$ mag for NGC 4592. Applying Jang et al. (2020) TRGB calibration, we derive distances: 9.28 ± 0.29 ($stat$) ± 0.26 (sys) Mpc for NGC 4437 and 9.07 ± 0.10 ($stat$) ± 0.25 (sys) Mpc for NGC 4592 (Table 2). These distance estimates are almost the same as those based on the Freedman et al. (2020) calibration, as listed in Table 2.

3.4. *Summary of TRGB Distance Estimation*

We used three different methods to obtain the TRGB distances of NGC 4437 and NGC 4592. Table 2 lists a summary of TRGB distance measurements derived from the three methods. Here we briefly compare the three methods. Since the observed LFs of NGC 4437 and NGC 4592 are different, we compare each method for each of the two cases.

The LF of NGC 4437 does not show a sharp edge due to the large slope of the AGB LF and a weak TRGB discontinuity. This makes the parameterization of the LF difficult. For instance, there were several local maxima when using the maximum likelihood method. Thus we tried the fitting with a number of initial conditions to find the true maximum. For the same reason, it was difficult to construct an ASLF that resembles the observed LF when using the GLOESS edge detection method. Since the TRGB discontinuity derived in the maximum likelihood method is small, we set a large ratio of AGB stars to RGB stars in the ASLF. This might have resulted in a larger uncertainty value for the GLOESS edge detection method. Compared to the complexity of these methods, the direct edge detection method is the simplest. However, a systematic uncertainty might be introduced because of a fixed bin size of the LF. While the GLOESS edge detection method estimates the systematic and random uncertainties using the ASLF and finds an optimal smoothing scale that minimizes the quadratic sum of systematic and random errors, the direct edge detection method does not include this procedure.

On the other hand, the LF of NGC 4592 clearly shows a sharp edge. The maximum likelihood method stably finds the maximum, and the ASLF is easily constructed. However, as seen in Figure 3(d), a false peak exists at $F814W \approx 26.1$ mag. While the GLOESS method suppresses this false edge, the direct edge detection method does not. Thus, the uncertainty of the direct edge de-

tection method is slightly larger than those of the other two methods.

In conclusion, the TRGB distance measurements derived from the three methods coincide well within the error range. It does not matter which of the three is used, but we adopt the results of the maximum likelihood method for the following analysis. This is because TRGBs of most galaxies in our Virgo infall sample (§4) are obtained with the maximum likelihood method. TRGBs of only five galaxies in the Tikhonov & Galazutdinova (2020) sample are measured with the edge detection method used in Lee et al. (1993). All the others are derived using the maximum likelihood method. Therefore, in order to be consistent, we chose the results of the maximum likelihood method.

In addition, our results show that distances to NGC 4437 and NGC 4592 are very similar. The spatial separation between the two is discussed in Section 5.1.

3.5. *Comparison with Previous TRGB Magnitude for NGC 4437*

Karachentsev et al. (2014) used the maximum likelihood analysis for TRGB detection and obtained $F814W_{\rm TRGB} = 25.65^{+0.16}_{-0.12}$ mag for NGC 4437. The resulting distance is 10% smaller than our measurement but is consistent considering the large error range presented. As discussed above, NGC 4437 shows an ambiguous tip in the maximum likelihood analysis. However, the edge response function we derived in Figure 3 shows a blunt but single peak at $F814W_{\rm TRGB} \sim 25.8$ mag, showing no peak at the TRGB magnitude proposed by Karachentsev et al. (2014). Therefore, we adopt our value for NGC 4437 for the following analysis.

4. VIRGO INFALL

4.1. *Virgo Infall Galaxy Sample*

Combining our results for NGC 4437 and NGC 4592 with those in the literature, we prepare a list of galaxies located between the Virgo cluster and the Local Group for which TRGB distances are available. We mainly use the sample of Virgo infall galaxies from Karachentsev et al. (2018) and add several galaxies from the literature that satisfy the selection criterion presented in Karachentsev et al. (2018). As will be discussed in Section 4.3, an ambiguity is introduced when transforming observed velocities into Virgocentric velocities. This ambiguity is a function of λ, which is defined as the angle between the line of sight toward a galaxy and the line connecting the galaxy with the cluster center. If a galaxy is located at the line-of-sight direction toward the Virgo cluster ($\lambda = 180°$), the Virgocentric velocity

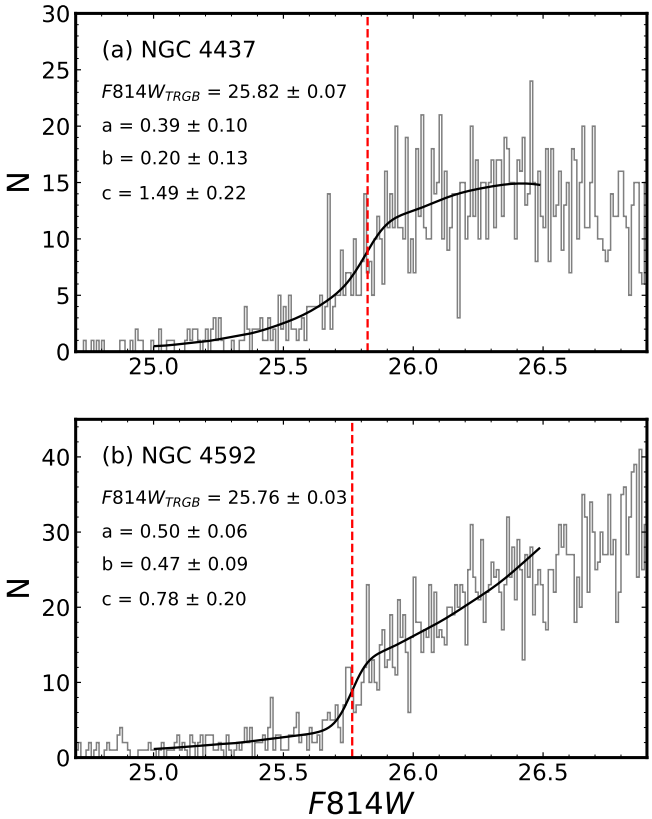

Figure 5. Results of maximum likelihood TRGB detection. Gray bars show 0.01 mag binned LF and black solid lines represent model LF convolved with photometric errors and incompleteness, $\varphi(m_{\rm TRGB}$, a, b, c). Red vertical lines mark the TRGB.

equals the line-of-sight velocity. However, the ambiguity increases as λ decreases. Therefore, Karachentsev et al. (2018) adopted a selection criterion of $\lambda = [135°, 180°]$.

In this study, we adopt $\lambda = [140°, 180°]$ in order to further reduce ambiguity. We adopt 25 galaxies from Karachentsev et al. (2018), excluding two galaxies with $\lambda = [135°, 140°]$. In this sample, TRGB magnitudes of 22 galaxies were obtained from the Extragalactic Distance Database (EDD)(Jacobs et al. 2009)[1], two galaxies (KK 177 and LVJ 1243+4127) are from Karachentsev et al. (2018), and one galaxy (AGC 749241) is from McQuinn et al. (2014). In addition, we find that five galaxies from Tikhonov & Galazutdinova (2020) satisfy $\lambda = [140°, 180°]$ and show Virgo infall motions: AGC 223231, AGC 223254, AGC 229379, AGC 238890, and AGC 742601. Moreover, NGC 4559 for which the TRGB magnitude is measured by McQuinn et al. (2017) also

[1] http://edd.ifa.hawaii.edu/

Table 2. A Summary of TRGB Distances

Galaxy	NGC 4437		NGC 4592	
TRGB Color	$(F606W - F814W)_{\rm ACS} = 1.23 \pm 0.10$		$(F555W - F814W)_{\rm WFC3} = 1.68 \pm 0.06$	
TRGB Magnitudes	$F814W_{\rm ACS}$		$F814W_{\rm WFC3}$	
GLOESS Edge Detection (Hatt et al. 2017)	25.811 ± 0.097		25.756 ± 0.033	
Direct Edge Detection (Jang & Lee 2017b)	25.829 ± 0.049		25.763 ± 0.050	
Maximum Likelihood (Makarov et al. 2006)	25.824 ± 0.072		25.765 ± 0.034	
	Calibration			
Distances	Jang et al. (2020)	Freedman et al. (2020)	Jang et al. (2020)	Freedman et al. (2020)
GLOESS Edge Detection (Hatt et al. 2017)	9.22 ± 0.47	9.24 ± 0.46	9.03 ± 0.27	9.04 ± 0.23
Direct Edge Detection (Jang & Lee 2017b)	9.30 ± 0.32	9.32 ± 0.29	9.06 ± 0.31	9.07 ± 0.28
Maximum Likelihood (Makarov et al. 2006)	9.28 ± 0.39	9.30 ± 0.36	9.07 ± 0.27	9.08 ± 0.24

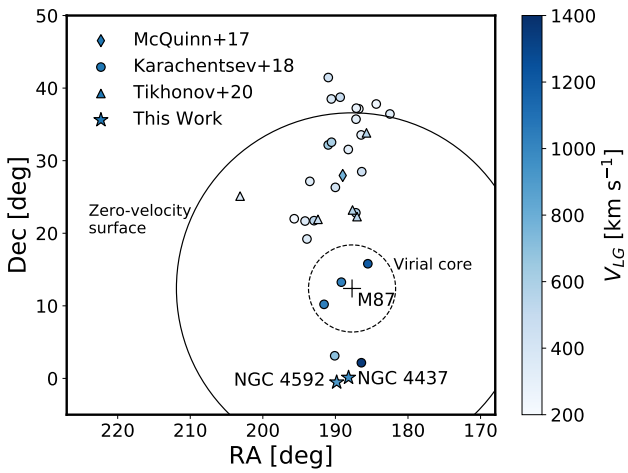

Figure 6. Map of the galaxies used for Virgo infall fitting. Colors represent line-of-sight velocities with respect to the Local Group. Note that the corresponding velocity of the Virgo cluster is 988km s^{-1} . Lines show the radius of the zero-velocity surface (with a radius of 24°) and the virial radius (with a radius of 6°).

satisfies the criteria. With our own measurements for NGC 4437 and NGC 4592, we compile TRGB magnitudes of 33 galaxies in total.

Table 3 shows a list of our sample galaxies. All the magnitudes in the table are in the HST/ACS filter system. The Johnson-Cousins V, I magnitudes in Tikhonov & Galazutdinova (2020) sample and the magnitudes of six galaxies observed by WFPC2 in EDD sample are transformed to $F606W_{\rm ACS}$ and $F814W_{\rm ACS}$ magnitudes using synthetic transformations obtained by Sirianni et al. (2005). For NGC 4592, the $(F555W - F814W)_{\rm WFC3}$ color is converted to the $(F555W - F814W)_{\rm ACS}$ color using the transformation in Jang & Lee (2015), then converted to the $(F606W - F814W)_{\rm ACS}$ color applying Eq. (1) in Jang & Lee (2017a). TRGB distances given in the table are derived using the Jang et al. (2020) calibration in order to maintain consistency. In calculating the error budget of TRGB distances, we consider the uncertainties of TRGB magnitudes provided in the literature, Jang et al. (2020) calibration error 0.055 mag, the magnitude transformation error 0.02 mag from Johnson-Cousins I-band to ACS for the Tikhonov & Galazutdinova (2020) sample (Sirianni et al. 2005), the zero-point error 0.07 mag of WFPC2 camera (Freedman et al. 2001), and the galactic extinction error (half of the extinction[2]). Radial velocities in the Local Group frame were obtained from NASA/IPAC Extragalacitc Database (NED)[3].

Spatial distributions of the galaxies used in this study are shown in Figure 6. The cross mark denotes the location of M87, the approximate dynamical center of the Virgo cluster. The radius of the virial core ($R \sim 6°$(Hoffman et al. 1980)) of the Virgo cluster is marked as the dashed line circle and the zero-velocity surface ($R \sim 24°$) as the solid line circle. Colors represent radial velocities in the Local Group frame. Galaxies are mainly distributed along the north-south direction. It is noted that NGC 4437 and NGC 4592 are rare infall examples in the southern region of the Virgo cluster. Galaxies closer to M87 tend to have larger radial velocities than those farther from M87, showing infall motion toward the Virgo center.

4.2. *Theoretical Description of the Virgo Infall Model*

Peirani & de Freitas Pacheco (2006, 2008) derived the velocity-distance relations of a spherical shell of radius

[2] The foreground extinction corrections for the sample galaxies are reasonably small ($A_{F814W} < 0.05$), as listed in Table 3. We adopt a conservative estimate of errors, taking half of A_{F814W}, considering a systematic uncertainty of the extinction map (e.g., $\sigma_{E(B-V)} \approx 0.03$ in Schlegel et al. (1998)).

[3] https://ned.ipac.caltech.edu/

Table 3. Virgo Infall Galaxy Sample

Name	R.A.(J2000) [°]	Decl.(J2000) [°]	Camera	$(F606W - F814W)_{\rm TRGB}$ [a] [mag]	$F814_{\rm TRGB}$ [b] [mag]	$D_{\rm TRGB}$ [c] [Mpc]	$A_{\rm F814W}$ [mag]	$R_{\rm VC}$ [d] [Mpc]	$V_{\rm LG}$ [e] [km s^{-1}]	$V_{\rm VC,mi}$ [km s^{-1}]	$V_{\rm VC,ma}$ [km s^{-1}]	λ [°]
UGC 07512	186.422208	2.158972	ACS	$1.33\ ^{+0.05}_{-0.02}$ (1)	26.35 ± 0.08 (1)	11.87 ± 0.53	0.03	5.26	1354 ± 6	−217	−461	146
VCC 2037	191.563750	10.205556	ACS	$1.69\ ^{+0.14}_{-0.01}$ (1)	$25.99\ ^{+0.21}_{-0.19}$ (1)	$10.01\ ^{+1.00}_{-0.91}$	0.04	6.56	1038 ± 1	−37	−54	169
IC 3583	189.181208	13.259331	ACS	1.79 ± 0.04 (1)	26.00 ± 0.05 (1)	9.92 ± 0.34	0.07	6.58	1034 ± 7	−44	−46	176
GR 34	185.531542	15.799111	ACS	$1.69\ ^{+0.11}_{-0.19}$ (1)	$25.91\ ^{+0.29}_{-0.16}$ (1)	$9.64\ ^{+1.31}_{-0.75}$	0.04	6.90	1206 ± 8	−205	−223	170
NGC 4437	188.189958	0.115028	ACS	1.23 ± 0.10 (3)	25.82 ± 0.07 (6)	9.28 ± 0.40	0.04	7.68	972 ± 5	90	−7	153
NGC 4600	190.095662	3.117750	ACS	1.27 ± 0.05 (1)	25.78 ± 0.06 (1)	9.07 ± 0.34	0.04	7.69	697 ± 2	318	297	159
NGC 4592	189.828067	-0.532008	WFC3	1.17 ± 0.06 (3)	25.77 ± 0.03 (6)	9.07 ± 0.27	0.03	7.93	912 ± 3	150	57	152
NGC 4559	188.990196	27.959992	ACS	1.17 ± 0.10 (4)	25.72 ± 0.04 (5)	8.87 ± 0.30	0.03	8.30	780 ± 2	287	203	148
NGC 4656	190.990542	32.168139	ACS	1.04 ± 0.01 (1)	25.43 ± 0.04 (1)	7.80 ± 0.25	0.02	9.55	644 ± 1	430	353	144
AGC 223231	185.719625	33.828528	ACS	0.97 ± 0.08 (4)	25.38 ± 0.10 (4)	7.64 ± 0.42	0.02	9.79	568 ± 1	500	447	142
AGC 229379	187.641675	23.205539	ACS	1.05 ± 0.11 (4)	25.13 ± 0.10 (4)	6.78 ± 0.37	0.03	9.92	571	438	421	162
NGC 4631	190.533375	32.541500	ACS	1.33 ± 0.01 (1)	25.31 ± 0.02 (1)	7.36 ± 0.20	0.03	9.93	604 ± 3	462	395	145
NGC 4455	187.183808	22.820447	ACS	$1.13\ ^{+0.02}_{-0.04}$ (1)	25.06 ± 0.07 (1)	6.54 ± 0.27	0.03	10.12	588 ± 1	420	402	163
AGC 742601	192.403542	21.917806	ACS	1.14 ± 0.09 (4)	25.04 ± 0.09 (4)	6.42 ± 0.32	0.05	10.25	472 ± 3	531	523	163
AGC 223254	187.020042	22.290167	ACS	1.16 ± 0.06 (4)	25.01 ± 0.10 (4)	6.39 ± 0.34	0.03	10.26	543 ± 4	461	448	164
IC 3840	192.942083	21.735194	ACS	1.05 ± 0.02 (1)	24.85 ± 0.06 (1)	5.86 ± 0.22	0.06	10.79	536 ± 3	469	454	163
KK 144	186.371458	28.482444	ACS	0.99 ± 0.02 (1)	24.82 ± 0.06 (1)	5.85 ± 0.22	0.04	11.00	453 ± 2	566	546	155
AGC 749241	190.007775	26.321183	ACS	$0.99\ ^{+0.02}_{-0.08}$ (4)	24.66 ± 0.06 (3)	5.47 ± 0.20	0.02	11.26	418 ± 1	591	579	159
Arp 211	189.340833	38.743889	ACS	$1.06\ ^{+0.04}_{-0.01}$ (1)	24.87 ± 0.07 (1)	6.02 ± 0.25	0.02	11.41	484 ± 2	590	523	140
AGC 238890	203.134583	25.114167	ACS	1.19 ± 0.07 (4)	24.48 ± 0.12 (4)	5.03 ± 0.32	0.02	11.89	356 ± 10	664	650	152
KDG 215	193.921000	19.209083	ACS	0.94 ± 0.02 (1)	24.33 ± 0.07 (1)	4.68 ± 0.19	0.03	11.90	362 ± 7	633	629	167
KK 177	195.674463	21.997394	ACS	1.10 ± 0.01 (2)	24.39 ± 0.04 (2)	4.75 ± 0.15	0.06	11.90	228 ± 2	767	772	163
DDO 133	188.226625	31.541111	WFPC2	1.05 ± 0.02 (1)	24.43 ± 0.05 (1)	4.90 ± 0.24	0.03	11.97	320 ± 1	694	688	153
NGC 4826	194.181838	21.682969	ACS	1.48 ± 0.02 (1)	24.26 ± 0.03 (1)	4.46 ± 0.13	0.06	12.15	365 ± 1	634	627	165
NGC 4395	186.453592	33.546928	ACS	1.30 ± 0.01 (1)	24.36 ± 0.01 (1)	4.75 ± 0.12	0.03	12.18	314 ± 1	705	696	151
DDO 126	186.771458	37.142583	WFPC2	1.01 ± 0.02 (1)	24.44 ± 0.07 (1)	4.93 ± 0.26	0.02	12.19	232 ± 2	783	808	145
PGC 038685	182.485292	36.434333	WFPC2	$1.07\ ^{+0.01}_{-0.03}$ (1)	24.42 ± 0.13 (1)	4.87 ± 0.36	0.04	12.23	341 ± 40	692	674	146
UGC 07605	187.161438	35.717481	WFPC2	$0.96\ ^{+0.03}_{-0.09}$ (1)	$24.33\ ^{+0.13}_{-0.11}$ (1)	$4.69\ ^{+0.35}_{-0.30}$	0.02	12.33	317 ± 1	708	696	148
DDO 127	187.119000	37.233639	WFPC2	$0.97\ ^{+0.01}_{-0.03}$ (1)	24.35 ± 0.07 (1)	4.72 ± 0.25	0.03	12.37	292 ± 5	734	730	146
LVJ 1243+4127	190.982083	41.456944	ACS	1.15 ± 0.02 (2)	24.36 ± 0.09 (2)	4.75 ± 0.23	0.03	12.56	444 ± 3	631	545	140
IC 3687	190.562917	38.503333	WFPC2	1.04 ± 0.02 (1)	24.27 ± 0.08 (1)	4.56 ± 0.25	0.03	12.56	381 ± 2	665	621	144
DDO 154	193.521875	27.149639	ACS	0.98 ± 0.02 (1)	23.94 ± 0.03 (1)	3.94 ± 0.11	0.01	12.75	354 ± 2	654	638	159
NGC 4244	184.373583	37.807111	ACS	$1.21\ ^{+0.03}_{-0.05}$ (1)	24.13 ± 0.07 (1)	4.26 ± 0.18	0.03	12.78	256 ± 1	765	765	146

[a] TRGB $(F606W - F814W)_{ACS}$ colors. References: (1) EDD; (2) Karachentsev et al. (2018); (3) this study; (4) visually measured from CMDs.

[b] TRGB $F814W_{\rm ACS}$ magnitudes. References: (1) EDD; (2) Karachentsev et al. (2018); (3) McQuinn et al. (2014); (4) Tikhonov & Galazutdinova (2020); (5) McQuinn et al. (2017); (6) this study.

[c] TRGB distances calculated applying the Jang et al. (2020) calibration.

[d] Calculated for $D_C = 16.5$ Mpc

[e] Local Group rest-frame velocities from NED. For AGC 229379, adopted from Tikhonov & Galazutdinova (2020).

R moving radially in the gravitational field created by a mass M inside a shell, including the cosmological constant term. This is applicable to regions outside the virial core, where the assumption of purely radial velocities can be held. They numerically solved an equation of motion of a shell

$$\frac{d^2R}{dt^2} = -\frac{GM}{R^2} + \Omega_\Lambda H_0^2 R \quad (2)$$

to obtain the velocity and distance of the present age of the universe, assuming $\Omega_\Lambda = 0.7$.

We followed the same method but using $\Omega_\Lambda = 0.685$ in Planck Collaboration et al. (2020) instead of 0.7. Dimensionless variables $x = tH_0$, $y = R/R_0$, and $u = \dot{R}/H_0R_0$ are defined for calculation, where R_0 is the present radius of the zero-velocity surface. At the radius of zero-velocity surface, where the relative velocity with respect to the Virgo center is zero, the cluster is separated from the Hubble expansion. In addition, introducing the constant $A = 2GM/(H_0^2R_0^3)$, Eq. (2) can be rewritten as:

$$\frac{d^2y}{dx^2} = -\frac{A}{2y^2} + \Omega_\Lambda y \quad (3)$$

The value of A is determined from boundary conditions (see Peirani & de Freitas Pacheco (2008) for details), $A = 3.7094$ for $\Omega_\Lambda = 0.685$, yielding the expression of mass of the Virgo cluster within the zero-velocity surface as:

$$M = \frac{1.855}{G} \times H_0^2R_0^3 = 4.29 \times 10^{12} h^2 (\frac{R_0}{[\mathrm{Mpc}]})^3 M_\odot, \quad (4)$$

where h is the local Hubble constant in units of 100 km s^{-1} Mpc^{-1} and R_0 is the present radius of the zero-velocity surface in Mpc. Present velocity and distance solutions of Eq. (3) with various initial energies are well described by the form $u = -b/y^n + by$, where $b = 1.335$ and $n = 0.702$. The values of these parameters are similar to those given by Peirani & de Freitas Pacheco (2006, 2008).

From these results we derive a velocity-distance relation:

$$v = f(R) = -\frac{0.940H_0}{R^n}(\frac{GM}{H_0^2})^{(n+1)/3} + 1.335H_0R. \quad (5)$$

Once we have cluster-centric distances and velocities of galaxies around a cluster, we can determine H_0 and R_0 (or M) using this equation.

4.3. *Fitting the Virgo Infall Pattern*

In order to fit our data to the model in Equation (5), we first need to transform the measured distances and velocities of galaxies into Virgocentric distances and Virgocentric velocities. To determine the distance and velocity of the Virgo cluster, we use the catalog of galaxies around M87 (Kashibadze et al. 2020). We select 78 early-type galaxies that are located within the angular virial radius ($\theta < 6°$) and in the distance range of $12 < D[\mathrm{Mpc}] < 22$, derived from the surface brightness fluctuation (SBF) method. The distance distribution of the selected galaxies shows a significant concentration at $D \sim 16.5$ Mpc. From these galaxies we derive a mean distance $< D_C >= 16.5 \pm 0.1$ Mpc and a mean velocity $< V_C >_{LG}= 988 \pm 61$ km s^{-1}, which are adopted as the distance and velocity of Virgo for the following analysis. These values are similar to those in Kashibadze et al. (2018) and Karachentsev et al. (2018).

We calculate Virgocentric distances as $R_{VC}^2 = D_g^2 + D_C^2 - 2D_g \times D_C \times cos\Theta$, where Θ is the angular separation of a galaxy from the Virgo center (M87) and D_g is the TRGB distance of the galaxy. Due to our ignorance of tangential velocities of the galaxies, radial velocities are transformed into Virgocentric velocities assuming two extreme cases of the mass of the overdensity (Karachentsev & Nasonova 2010; Kashibadze & Karachentsev 2018). One is a minor attractor model where the peculiar velocities of satellite galaxies around a group or cluster are much smaller than the velocities of regular Hubble flow (see Figure 3 in Kashibadze & Karachentsev (2018)).

$$V_{VC,\mathrm{minor}} = V_g \times cos\lambda - V_c \times cos(\lambda + \Theta) \quad (6)$$

where V_g is the radial velocity of the galaxy in the Local group rest frame. The other is a major attractor model where satellite galaxies show significant infall motion toward the center of a galaxy group or cluster.

$$V_{VC,\mathrm{major}} = [V_g - V_C \times cos\Theta]/cos\lambda \quad (7)$$

The details of each model are described in Karachentsev & Nasonova (2010) and Kashibadze & Karachentsev (2018). Note that the difference between $V_{VC,\mathrm{minor}}$ and $V_{VC,\mathrm{major}}$ increases as λ deviates from 180°: galaxies with $\lambda = [140°, 160°]$ have an average difference of 50 km s^{-1} whereas those with $\lambda = [160°, 180°]$ have 10 km s^{-1}. True Virgocentric velocities are expected to lie between velocities transformed by the minor attractor model and the major attractor model.

Virgocentric distances and Virgocentric velocities of our galaxy sample are shown in Figure 7, (a) assuming the minor attractor model and (b) assuming the major attractor model. Compared with the unperturbed Hubble flow (gray lines), our sample galaxies show infall motions toward the Virgo cluster. $V_{VC,\mathrm{major}}$ values are generally smaller than $V_{VC,\mathrm{minor}}$ values for each galaxy.

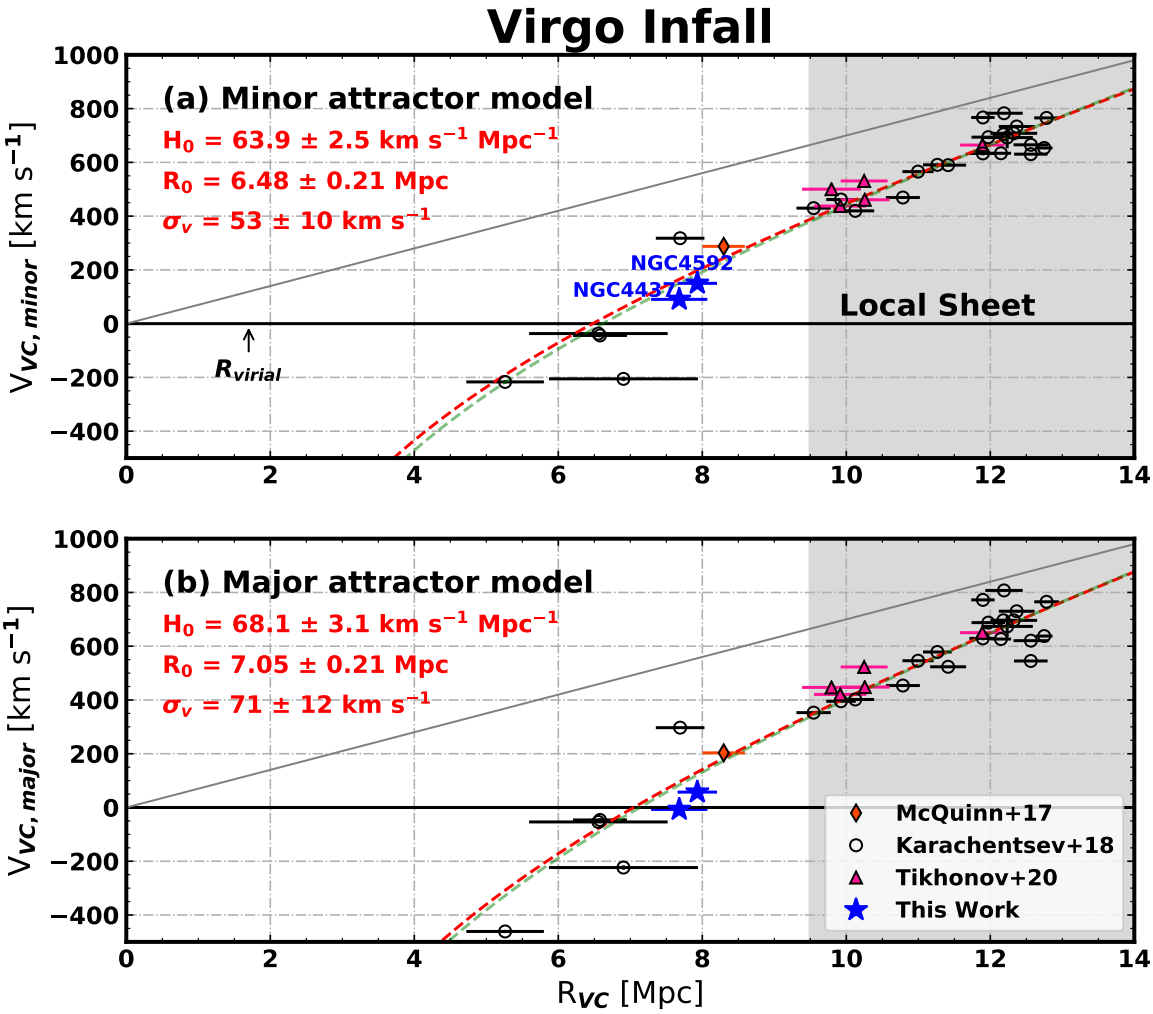

Figure 7. The Hubble diagram of the sample galaxies in the Virgo cluster frame: Virgocentric velocity vs. Virgocentric distance. Radial velocities are transformed into Virgocentric velocities using (a) the minor attractor model and (b) the major attractor model. NGC 4437 and NGC 4592, of which TRGB distances are measured in this study, are marked as blue starlets. Fitted models using the MCMC method and using the least-squares method are marked as red and green dashed lines, respectively. The gray straight lines represent the unperturbed Hubble flow for $H_0 = 70$ km s^{-1} Mpc^{-1}.

Note that the velocity scatter of galaxies in the Local Sheet ($D_g < 7$ Mpc (Tully et al. 2008), gray shaded region ($R_{VC} > 9.5$ Mpc)) is smaller than that of galaxies closer to the Virgo cluster.

Then we fit the Virgocentric distances and Virgocentric velocities of galaxies using the Bayesian approach. The likelihood of observing a galaxy at Virgocentric distance R_i given parameters H_0, R_0, and error σ is modeled as

$$p(v_i|R_i, H_0, R_0, \sigma) = \frac{1}{\sqrt{2\pi\sigma^2}} \exp\left(-\frac{(f(R) - v_i)^2}{2\sigma^2}\right) \tag{8}$$

where

$$\sigma^2 = err(v_i)^2 + err(R_i)^2 \times (\frac{\partial f}{\partial R})^2 + \sigma_v^2. \tag{9}$$

Here, $err(v)$ and $err(R)$ are measurement errors of velocity and distance. σ_v is an intrinsic velocity dispersion independent of measurement errors, which can be interpreted as a scatter due to peculiar motions. $\partial f/\partial R$ denotes the gradient of the model Hubble flow at given distance and parameters. Then the posterior probability

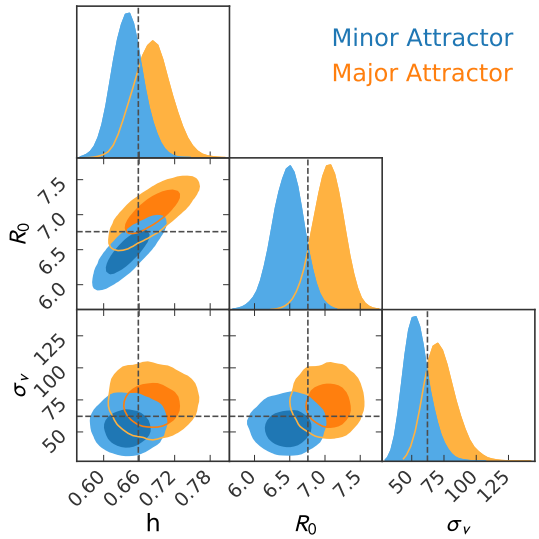

Figure 8. Posterior probability distributions for the parameters (h [100km s^{-1} Mpc^{-1}], R_0 [Mpc], σ_v [km s^{-1}]) estimated by minor (blue) and major (orange) attractor models. Two contour levels indicate 68% and 95% levels, respectively. Estimated parameter values and their errors are obtained from the median (dashed lines) and standard deviation of the sum of two posterior probability distributions.

distribution is given as

$$p(H_0, R_0, \sigma_v|v) \propto \prod_i p(v_i|H_0, R_0, \sigma_v) \times p(H_0, R_0, \sigma_v) \tag{10}$$

Here, we assume a uniform prior probability distribution ($p(H_0, R_0, \sigma_v)$) over 40 km s^{-1} Mpc^{-1}< H_0 < 90 km s^{-1} Mpc^{-1}, 3 Mpc < R_0 < 9 Mpc, and 10 km s^{-1}< σ_v < 200 km s^{-1}.

We use `emcee` (Foreman-Mackey et al. 2013), a python implementation of the ensemble sampler for MCMC. Values of the local Hubble constant H_0, the radius of zero-velocity surface R_0, and the intrinsic velocity dispersion σ_v are estimated from both the minor and major attractor models.

We also tried the least-squares fitting method for the comparison with Karachentsev et al. (2018). Karachentsev et al. (2018) used the least-squares fitting method for both the minor and major attractor models, and averaged the results to get mean values. We follow the same fitting method, but additionally conducted Monte Carlo simulations in order to estimate fitting errors. First, each data point (R_{VC}, V_{VC}) is shifted randomly 5000 times assuming a Gaussian distribution with standard deviation of measurement errors. Then H_0 and R_0 parameters are obtained 5000 times using the least-squares method. Uncertainties of the parameters are obtained from standard deviations of 5000 trials. Note that the intrinsic velocity dispersion σ_v is unable to be modeled using the least-squares method.

4.4. *Fitting Results*

The top panel in Table 4 lists the results of the MCMC fitting. Using $V_{VC,\mathrm{minor}}$ for v, we obtain $H_{0,\mathrm{minor}} = 63.9 \pm 2.5$ km s^{-1} Mpc^{-1} , $R_{0,\mathrm{minor}} = 6.48 \pm 0.21$ Mpc, and $\sigma_{v,\mathrm{minor}} = 53 \pm 10$ km s^{-1}. In addition, using $V_{VC,\mathrm{major}}$ for v, we get $H_{0,\mathrm{major}} = 68.1 \pm 3.1$ km s^{-1} Mpc^{-1} , $R_{0,\mathrm{major}} = 7.05 \pm 0.21$ Mpc, and $\sigma_{v,\mathrm{major}} = 71 \pm 12$ km s^{-1}. The rms errors of the fit are 73 km s^{-1} and 84 km s^{-1} , respectively. All the parameters H_0, R_0, and σ_v are slightly larger for the major attractor model than those of the minor attractor model. The fitted lines are shown as red dashed lines in Figure 7. Figure 8 displays the posterior probability distributions of the parameters for both minor and major attractor models.

The bottom panel in Table 4 and the green dashed lines in Figure 7 show the results of the least-squares fitting. The values of the parameters derived using this method are slightly ($\sim 1.5\%$) larger than those obtained using the MCMC method, but they are consistent within the error range.

Since the minor and major attractor models are two extreme cases, it is likely that the true values lie between parameter values estimated by the two models. We sum probability distributions obtained from two cases (histograms in Figure 8), and derive median values and standard errors from these. In doing so, errors of the parameters are conservatively estimated. We obtain average parameter values as $H_0 = 65.8 \pm 3.5$ km s^{-1} Mpc^{-1}, $R_0 = 6.76 \pm 0.35$ Mpc, and $\sigma_v = 62 \pm 14$ km s^{-1}(right column of Table 4). The implications of H_0 will be discussed in Section 5.3. Here, we briefly discuss our results of R_0, rms errors of the fit, and σ_v.

We calculate the mass of the Virgo cluster within R_0 with Equation (4), obtaining $M(R_0) = (5.7 \pm 1.5) \times 10^{14} M_\odot$. This value is very similar to the virial mass estimate, $M_{vir} = (6.3 \pm 0.9) \times 10^{14} M_\odot$ for the virial radius of 1.7 Mpc, derived from velocity dispersion of all types of galaxies by Kashibadze et al. (2020). Assuming that only early-type galaxies are in the relaxed state and adopting the velocity dispersion of these galaxies, they derived a slightly smaller value, $M_{vir} = 4.1 \times 10^{14} M_\odot$. Our estimation of $M(R_0)$ lies between the two values, suggesting that $M(R_0) \sim M_{vir}$. This confirms that the outer region of the Virgo cluster core does not contain a considerable amount of dark matter, as suggested by previous studies (Karachentsev et al. 2014, 2018; Kashibadze et al. 2018, 2020).

Among the previous studies that estimated R_0, Karachentsev et al. (2018) fitted TRGB distances and

velocities of the galaxies in front of the Virgo cluster to the velocity-distance relation but they used a slightly different form from ours, which will be described in Section 5.3. They obtained $R_0 = 7.3 \pm 0.3$ Mpc and the mass of the Virgo cluster within R_0 as $M(R_0) = (7.64 \pm 0.91) \times 10^{14} M_\odot$ where Planck model parameters (Planck Collaboration et al. 2020) are used. Our results are slightly smaller than those of Karachentsev et al. (2018). This is mainly because the fitting methods and the adopted distances of the Virgo cluster are different in the two studies. The value of R_0 obtained by the least-squares method in this study is slightly closer to the value of R_0 in Karachentsev et al. (2018). In addition, the adopted distance of the Virgo cluster in Karachentsev et al. (2018) is 16.65 Mpc, 0.15 Mpc larger than the value in this study, accounting for the larger value of R_0. The error in our study is larger than the error given by Karachentsev et al. (2018). This is because we include the error of both H_0 and R_0, while Karachentsev et al. (2018) include only the error of R_0.

We compare the rms velocity errors (or observed velocity dispersions) in this study (73 km s^{-1} and 84 km s^{-1} for the minor and major attractor models) to those in the previous studies. Peirani & de Freitas Pacheco (2008) obtained the velocity dispersion as 345 km s^{-1} by fitting velocities and Tully-Fisher distances of 27 galaxies in the Virgo infall region. This value is much larger than those in this study. The large uncertainties in Tully-Fisher distances might have attributed to their large values. In fact, Karachentsev et al. (2018) suggested a much smaller velocity dispersion by using only the galaxies with TRGB distances to fit the Virgo infall pattern. They obtained the velocity dispersion to be 92 km s^{-1} and 105 km s^{-1} for the minor and major attractor models, mentioning that the Hubble flow around the Virgo cluster is cold. Our velocity dispersion values based on the larger sample are even smaller (by about 20%) than those of Karachentsev et al. (2018), supporting the coldness of the Hubble flow.

The intrinsic velocity dispersion, σ_v, is a useful quantity, which can be interpreted as the velocity dispersion minus the dispersion contributed by measurement errors. We obtain $\sigma_v = 62 \pm 14$ km s^{-1}, which is about 80% of the rms errors. This shows that the Hubble flow around Virgo is even colder than suggested in the previous studies (Karachentsev et al. 2018): 78 km s^{-1} and 90 km s^{-1} for the minor and major attractor models. The value for Virgo is about 1.6 times larger than the σ_v derived from the Local Group Hubble flow, $\sigma_v = 38$ km s^{-1}(Peñarrubia et al. 2014).

5. DISCUSSION

5.1. *The NGC 4437 Group*

Two previous studies classified NGC 4437 and NGC 4592 as a galaxy group, but the separation of the two galaxies was considered large, lacking grounds for their membership (Tully et al. 2013; Karachentsev & Nasonova 2013). Tully et al. (2013) grouped NGC 4437 with NGC 4592 and another galaxy NGC 4544 using redshift information, and presented their weighted average of existing distance measurements to be 8.58, 11.69, and 18.11 Mpc respectively. Given the faintness of NGC 4437 ($M_{B_T} = -18.7$ mag (de Vaucouleurs et al. 1991), about an order of magnitude fainter than M31), their separations are too large for them to be considered as a group. Karachentsev & Nasonova (2013) studied galaxies in the southern part of the Virgo cluster and identified NGC 4437, NGC 4592, and CGCG 014-054 as a foreground galaxy group. They adopted their Tully-Fisher distances as 9.7, 11.6, and 9.6 Mpc, respectively. However, the separations between NGC 4592 and other galaxies are too large for them to be considered as a group.

As presented in Section 3, our distances to NGC 4437 and NGC 4592 are very similar, showing that they are spatially adjacent. Their three-dimensional spatial separation is only 0.29 Mpc and its 1σ range is [0.26, 0.59] Mpc. We conclude that they are indeed a physical pair located close to the zero-velocity surface of the Virgo cluster ($R_0 = 6.76 \pm 0.35$ Mpc). In fact, we measured SBF distances to dwarf galaxies found in a wide HSC $5^\circ \times 5^\circ$ image centered on NGC 4437 and found five dwarf galaxies to be located at distances similar to NGC 4437 and NGC 4592, implying that they are probable members of the NGC 4437 group. These results will be presented in the future paper (Kim et al. (2020) in preparation).

5.2. *Systematic Uncertainties of H_0*

There are at least four kinds of systematic uncertainties present in our method for obtaining H_0: (1) uncertainties from velocity-distance models, (2) uncertainties due to ignorance of tangential velocities, (3) zero-point uncertainties in the TRGB measurement, and (4) uncertainties in the distance and velocity of the Virgo cluster. In this Section, we describe possible sources of systematic uncertainties in our H_0 determination.

First, our method is model-dependent. The velocity-distance model assumes a spherically symmetric mass distribution of the Virgo cluster, which is a simplified model. However, we conjecture that the uncertainties arising from the imperfect model are not significant. Peñarrubia et al. (2014) carried N-body experiments of the Hubble flow perturbed by the Local Group, us-

Table 4. Virgo Infall Fitting Results

	Minor Attractor	Major Attractor	Average
MCMC			
H_0 [km s^{-1} Mpc^{-1}]	63.9 ± 2.5	68.1 ± 3.1	65.8 ± 3.5
R_0 [Mpc]	6.48 ± 0.21	7.05 ± 0.21	6.76 ± 0.35
σ_v [km s^{-1}]	53 ± 10	71 ± 12	62 ± 14
RMS [km s^{-1}]	72.9	83.6	
Virgo Mass [M$_\odot$]	$(4.8 \pm 0.8) \times 10^{14}$	$(7.0 \pm 1.3) \times 10^{14}$	$(5.7 \pm 1.5) \times 10^{14}$
Least-Squares + Monte-Carlo			
H_0 [km s^{-1} Mpc^{-1}]	65.1 ± 2.4	68.9 ± 2.8	66.8 ± 3.2
R_0 [Mpc]	6.62 ± 0.22	7.13 ± 0.21	6.86 ± 0.33
RMS [km s^{-1}]	71.2	82.6	
Virgo Mass [M$_\odot$]	$(5.3 \pm 0.9) \times 10^{14}$	$(7.4 \pm 1.3) \times 10^{14}$	$(6.2 \pm 1.4) \times 10^{14}$

ing two mass distribution models: central point mass and a pair of point masses (corresponding to the Milky Way and M31). They determined the mass of the Local Group and cosmological constants from synthetic data generated with both models. Although different mass distribution models resulted in different values of the Local Group mass, the values of the Hubble constant remained unchanged. This implies that the possible asymmetric mass distribution in the core of the Virgo cluster might not influence the value of H_0 significantly. Moreover, since there are neither conspicuous large-scale structures nor massive galaxy groups between the Local Group and the Virgo cluster, it is likely that the Hubble constant is not biased due to mass distributions in the outskirts.

Nevertheless, the model fitting range may introduce systematic uncertainties. The model should be applied to the galaxies that have been under the influence of gravitational force exerted by the Virgo mass M from the early universe. That is, galaxies in the outer region might not follow the model. Thus, it is crucial to restrict the fitting range of distances. In fact, Nasonova et al. (2011) fitted the velocity-distance relation using velocities and distances of galaxies in front of the Fornax cluster, which are located at $R_{\rm Fornax} < R_{\rm max}$ where $R_{\rm max}H_0 = v(R_{\rm max})$. $R_{\rm max}$ is approximately 2.2 times the radius of zero-velocity surface. By this criterion, they separated infalling galaxies that follow the velocity-distance relation (Eq. (5)) and other galaxies that follow Hubble expansion only. All of our 33 galaxies are located at $R_{VC} < 1.9R_0$, so it can be considered reasonable to assume that they have been in the infall region from the early universe. Still, the true border is ambiguous and we cannot exclude a possibility that the criterion could be modified.

Second, we conjectured that the true H_0 is likely to lie in between $H_{0,\rm minor}$ and $H_{0,\rm major}$. Since tangential velocities of the galaxies are not available, radial velocities are transformed into Virgocentric velocities assuming two extreme cases. H_0 is diminished to 63.9 ± 2.5 km s^{-1} Mpc^{-1} when the minor attractor model is true, and H_0 is increased to 68.1 ± 3.1 km s^{-1} Mpc^{-1} when the major attractor model is true. The uncertainty due to ambiguous velocity transformation is reflected into the error range (± 3.5 km s^{-1} Mpc^{-1}) we derived in this study.

Table 5. H_0 [km s^{-1} Mpc^{-1}] for Different Ranges of λ

λ range	N	Minor Attractor	Major Attractor	Average
$\lambda > 140°$	33	63.9 ± 2.5	68.1 ± 3.1	65.8 ± 3.5
$\lambda > 145°$	27	65.8 ± 2.6	70.6 ± 3.1	68.1 ± 3.7
$\lambda > 150°$	20	65.3 ± 3.6	67.8 ± 4.2	66.4 ± 4.1
$\lambda > 155°$	15	63.3 ± 4.8	63.2 ± 5.0	63.2 ± 4.9

One method of reducing systematic uncertainties arising from the different velocity transformation models is using only the galaxies with high λ. In Table 5 we present H_0 values obtained from different constraints on λ. As expected, using more stringent ranges for λ results in the gaps between H_0s of the minor attractor model and the major attractor model decreasing, but shows larger random errors due to smaller sample size. Using $\lambda > 145°$ or $\lambda > 150°$, H_0s increase both for the minor and major attractor models, but not significantly considering random errors. The standard deviation of four H_0s using different ranges of λ is ∼2.0 km s^{-1} Mpc^{-1}. Although systematic uncertainty decreases when using a smaller number of galaxies with larger λ, the increase of random error becomes significant. Thus we adopt $\lambda > 140°$ for our final results.

Third, our H_0 determination is subject to uncertainties of TRGB calibration. Quadratic sum of the statis-

tical uncertainty and the systematic uncertainty in the TRGB calibration of Jang et al. (2020) is 0.055 mag. This results in ± 1.1 km s^{-1} Mpc^{-1} uncertainty in H_0. We also test H_0 determination using different calibrations. Using the calibration of Freedman et al. (2020) anchored on the distance to the Large Magellanic Cloud, we obtain $H_{0,\mathrm{minor}} = 64.0 \pm 2.5$ km s^{-1} Mpc^{-1} and $H_{0,\mathrm{major}} = 68.4 \pm 3.1$ km s^{-1} Mpc^{-1} , yielding $H_0 = 66.0 \pm 3.5$ km s^{-1} Mpc^{-1}.

In addition, given that TRGB colors of a few galaxies in our sample marginally belong to the blue, constant TRGB magnitude range, we use calibrations by Rizzi et al. (2007) and Jang & Lee (2017a) as well. Rizzi et al. (2007) obtained a linear relation between TRGB colors and F814W TRGB magnitudes. Using their calibration, we obtain $H_{0,\mathrm{minor}} = 66.6 \pm 2.7$ km s^{-1} Mpc^{-1} and $H_{0,\mathrm{major}} = 71.6 \pm 3.0$ km s^{-1} Mpc^{-1} , yielding $H_0 = 69.0 \pm 3.8$ km s^{-1} Mpc^{-1}. Moreover, Jang & Lee (2017a) presented a quadratic relation between RGB colors and TRGB magnitudes. Adopting their calibration using NGC 4258 as a distance anchor with the zero-point replaced with the updated value from Jang et al. (2020), we get $H_{0,\mathrm{minor}} = 64.2 \pm 2.5$ km s^{-1} Mpc^{-1} and $H_{0,\mathrm{major}} = 68.3 \pm 3.1$ km s^{-1} Mpc^{-1} , resulting in $H_0 = 66.1 \pm 3.5$ km s^{-1} Mpc^{-1}. Thus, all these values from different calibrations agree within errors.

Lastly, the H_0 determination depends on the distance and velocity of the Virgo cluster. Adopting the values as $< D_C >= 16.5 \pm 0.1$ Mpc and $< V_C >_{LG}= 988 \pm 61$ km s^{-1} , and assuming Gaussian error distributions, we calculate systematic errors using the Monte Carlo approach. The smaller the D_C, the larger the H_0: ± 0.1 Mpc uncertainty of D_C results in ∓ 0.2 km s^{-1} Mpc^{-1} uncertainty in H_0. In addition, the larger the V_C, the larger the H_0: ± 61 km s^{-1} uncertainty of V_C results in ± 2.1 km s^{-1} Mpc^{-1} uncertainty in H_0. Thus, combined with the calibration uncertainty (± 1.1 km s^{-1} Mpc^{-1}) described above, the total systematic uncertainty is 2.4 km s^{-1} Mpc^{-1} , resulting in $H_0 = 65.8 \pm 3.5(stat) \pm 2.4(sys)$ km s^{-1} Mpc^{-1}. The calculated error budgets are summarized in Table 6.

Table 6. Error Budget of H_0 [km s^{-1} Mpc^{-1}]

Parameter	Minor Attractor	Major Attractor	Average
Random (Fitting)	2.5	3.1	3.5[a]
Systematic			
TRGB Calibration	1.2	1.0	1.1
$< D_C >$	0.1	0.2	0.2
$< V_C >_{LG}$	2.1	2.2	2.1
Systematic Total	2.5	2.4	2.4

[a] The uncertainty due to the ambiguous velocity transformation is reflected into the error range of the average value.

5.3. *The Local H_0*

We estimate a local Hubble constant $H_0 = 65.8 \pm 3.5(stat) \pm 2.4(sys)$ km s^{-1} Mpc^{-1} , with 6% uncertainty using 33 galaxies located between the Virgo cluster and the Local Group. In this Section, we first compare our H_0 result with those of previous studies using Virgo infall. Then we compare our H_0 with those from other recent methods from the literature.

Peirani & de Freitas Pacheco (2006) fitted 27 galaxies in front of the Virgo cluster with Tully-Fisher distances (Teerikorpi et al. 1992) to the velocity-distance relation and obtained $H_0 = 65 \pm 9$ km s^{-1} Mpc^{-1}, which was revised in Peirani & de Freitas Pacheco (2008) to $H_0 = 71 \pm 9$ km s^{-1} Mpc^{-1}. This value is consistent with the one in this study. However, it is noted that, with increased accuracy in distance measurements in this study, H_0 is determined with a much smaller error, about half of the previous studies.

More recently, Karachentsev et al. (2018) fitted 28 galaxies with TRGB distances to the velocity-distance model by Peñarrubia et al. (2014); Peñarrubia, & Fattahi (2017). The velocity-distance model of Peñarrubia et al. (2014) has the form for t_0 (the age of the universe):

$$v = (1.2 + 0.31\Omega_\Lambda)\frac{R}{t_0} - 1.1\sqrt{\frac{GM}{R}} \qquad (11)$$

If we set fixed $n = 0.5$ when fitting the numerical solution in Eq. (5) instead of setting it as a free parameter, our solution is expected to be similar to the above form. Karachentsev et al. (2018) modified this model by dropping the coefficients: $v = H_{0,\mathrm{Kar}}R - H_{0,\mathrm{Kar}}\sqrt{R_0^3/R}$. This resulted in a large value of $H_{0,\mathrm{Kar}}$, 97 km s^{-1} Mpc^{-1} for the minor attractor model and 104 km s^{-1} Mpc^{-1} for the major attractor model. They did not present the uncertainties of these values. Conversion of several variables and using $\Omega_\Lambda = 0.685$ in Eq. (11) yields $v = 1.48H_0R - 1.50H_0\sqrt{R_0^3/R}$, so that $H_{0,\mathrm{Kar}} \sim 1.49H_0$. Then the large Hubble constant in Karachentsev et al. (2018) reduces to $H_0 = 65$ km s^{-1} Mpc^{-1} for the minor attractor model and 70 km s^{-1} Mpc^{-1} for the major attractor model, which are coincident with our results.

Moreover, our H_0 agrees well with the very local value of $H_0 = 67 \pm 5$ km s^{-1} Mpc^{-1} determined by Peñarrubia et al. (2014) using the Local Group infall. They fitted velocities and TRGB distances of 34 galaxies in the Local Group to the theoretical infall model using Bayesian techniques in order to obtain cosmological parameters.

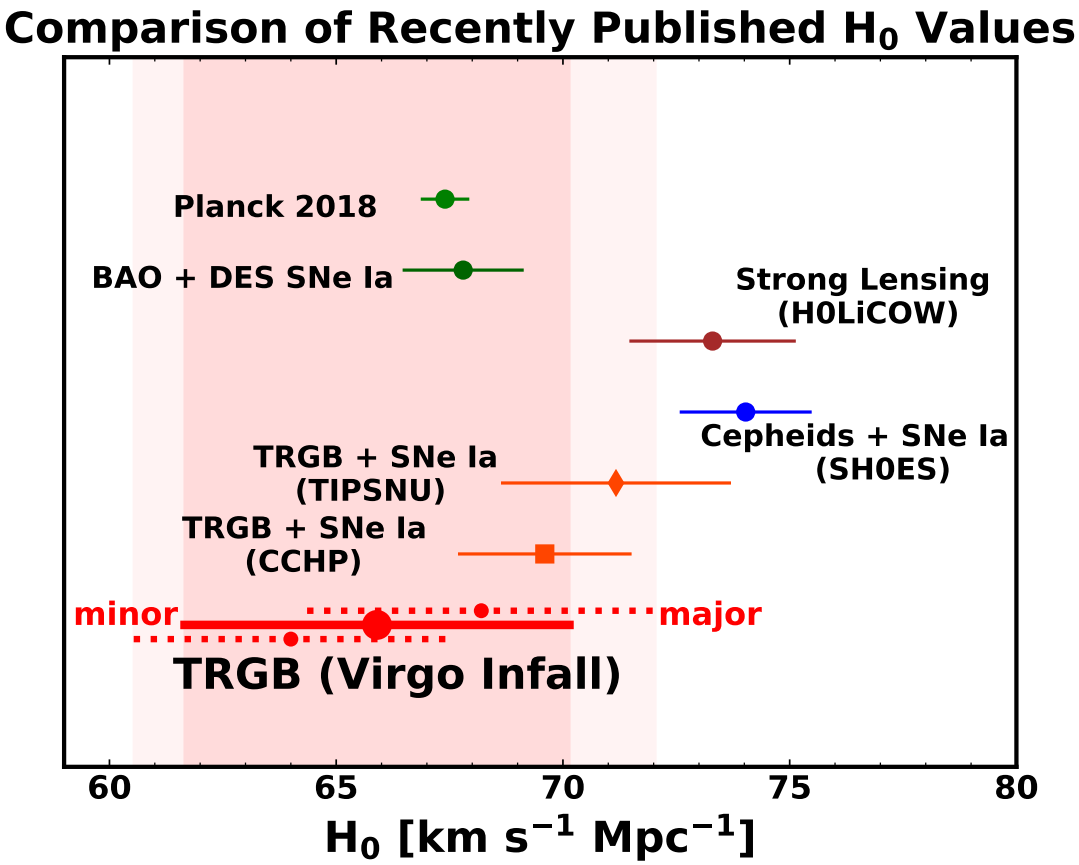

Figure 9. Comparison of H_0 obtained in this work (large red circle is the average, and small red circles are the minor and major attractor models) with other recent determinations (CMB: Planck Collaboration et al. (2020); DES SNe Ia + BAO: Macaulay et al. (2019); Strong Lensing: Wong et al. (2020); Cepheids + SNe Ia: Riess et al. (2019); TRGB + SNe Ia (TIPSNU): Jang & Lee (2017b), diamond symbol; TRGB + SNe Ia (CCHP): Freedman et al. (2020), square symbol) The horizontal bars indicate 1σ error range. The darker shaded region shows the 1σ error range of H_0 from the average of minor and major attractor models and the lighter shaded region shows 1σ ranges of $H_{0,\mathrm{minor}}$ and $H_{0,\mathrm{major}}$.

Finally, Figure 9 shows a comparison of our H_0 measurement with those based on other methods in the literature. First, our value of H_0 is consistent with the values derived from TRGB-calibrated SNe Ia (Jang & Lee 2017b; Freedman et al. 2020). This is remarkable, because they are derived from two totally independent methods based on the same TRGB distances. Second, our value of H_0 is consistent with the values of Planck (Planck Collaboration et al. 2020) and baryon acoustic oscillations (BAO) (Macaulay et al. 2019). Thus, our measurement shows little tension with the Planck value. Third, our value of H_0 is smaller than the value from Cepheid-calibrated SNe Ia (Riess et al. 2019), with the difference being at the level of 1.8σ.

6. SUMMARY

We obtained TRGB distances to NGC 4437 and NGC 4592 using resolved RGB stars present in the *HST* images. Then we compiled TRGB magnitudes of 33 galaxies located between the Local Group and the Virgo cluster, including our own measurements of NGC 4437 and NGC 4592. We determined the value of H_0 by fitting the distances and velocities of these 33 galaxies to the theoretical velocity-distance relation. Our main results are summarized as follows.

- We applied three different methods of TRGB detection to LFs of NGC 4437 and NGC 4592: the GLOESS method (Hatt et al. 2017), the direct edge detection method (Jang & Lee 2017a), and the maximum likelihood method (Makarov et al. 2006). All the measurements with different methods coincided well within their quoted uncertainties. The resulting TRGB distances are 9.28 ± 0.39 Mpc and 9.07 ± 0.27 Mpc for NGC 4437 and NGC 4592, respectively.

- The spatial separation between NGC 4437 and NGC 4592 is $0.29^{+0.30}_{-0.03}$ Mpc, implying that they are indeed a physical pair, consisting of a galaxy group. It is noted that they are located near the zero-velocity surface of the Virgo cluster.

- Including our own measurements, we compiled TRGB magnitudes of 33 galaxies located between the Local Group and the Virgo cluster. We found that the local Hubble flow perturbed by the Virgo cluster is well described by a velocity-distance relation as a function of cosmological constants (H_0, Ω_Λ) and R_0. By fitting velocities and distances of the galaxies to the relation using MCMC, we obtained $H_0 = 65.8 \pm 3.5(stat) \pm 2.4(sys)$ km s^{-1} Mpc^{-1} and $R_0 = 6.76 \pm 0.35$ Mpc.

- Our H_0 is in agreement with those obtained from TRGB-calibrated SNe Ia (Jang & Lee 2017b; Freedman et al. 2020). Moreover, our local H_0 is consistent with the Planck value (Planck Collaboration et al. 2020) measured from CMB. It is slightly smaller than the value from Cepheid-calibrated SNe Ia (Riess et al. 2019).

- Our estimation of the mass of the Virgo cluster within the zero-velocity surface is $M(R_0) = (5.7 \pm 1.5) \times 10^{14} M_\odot$, which is very similar to the virial mass. This confirms the conclusions of previous studies (Karachentsev et al. 2014, 2018; Kashibadze et al. 2018, 2020) that the outskirts of the Virgo cluster do not contain a significant amount of dark matter.

- The Hubble flow around the Virgo cluster is cold, as indicated by small values of rms velocity error of the fit and intrinsic velocity dispersion ($\sigma_v = 62 \pm 14$ km s^{-1}).

We thank the anonymous referee for useful suggestions. This work was supported by the National Research Foundation grant funded by the Korean Government (NRF-2019R1A2C2084019). J.K. was supported by the Global Ph.D. Fellowship Program (NRF-2016H1A2A1907015) of the National Research Foundation (NRF). We thank Brian S. Cho for his help in improving the English in this paper.

REFERENCES

Aihara, H., AlSayyad, Y., Ando, M., et al. 2019, PASJ, 71, 114

Bondi, H. 1947, MNRAS, 107, 410

de Vaucouleurs, G., de Vaucouleurs, A., Corwin, H. G., et al. 1991, Third Reference Catalogue of Bright Galaxies (RC3) (New York: Springer)

Dolphin, A. E. 2000, PASP, 112, 1383

Foreman-Mackey, D., Hogg, D. W., Lang, D., et al. 2013, PASP, 125, 306

Freedman, W. L., Madore, B. F., Gibson, B. K., et al. 2001, ApJ, 553, 47

Freedman, W. L., Madore, B. F., Hatt, D., et al. 2019, ApJ, 882, 34

Freedman, W. L., Madore, B. F., Hoyt, T., et al. 2020, ApJ, 891, 57

Gonzaga, S. & et al. 2012, The DrizzlePac Handbook, HST Data Handbook

Hatt, D., Beaton, R. L., Freedman, W. L., et al. 2017, ApJ, 845, 146

Hoffman, G. L., Olson, D. W., & Salpeter, E. E. 1980, ApJ, 242, 861

Jacobs, B. A., Rizzi, L., Tully, R. B., et al. 2009, AJ, 138, 332

Jang, I. S. & Lee, M. G. 2015, ApJ, 807, 133

Jang, I. S. & Lee, M. G. 2017a, ApJ, 836, 74

Jang, I. S., & Lee, M. G. 2017b, ApJ, 835, 28

Jang, I. S., Hatt, D., Beaton, R. L., et al. 2018, ApJ, 852, 60

Jang, I. S., Hoyt, T., Beaton, R., et al. 2020, arXiv:2008.04181

Kahn, F. D. & Woltjer, L. 1959, ApJ, 130, 705

Karachentsev, I. D., & Nasonova, O. G. 2010, MNRAS, 405, 1075

Karachentsev, I. D., & Nasonova, O. G. 2013, MNRAS, 429, 2677

Karachentsev, I. D., Makarov, D. I., & Kaisina, E. I. 2013, AJ, 145, 101

Karachentsev, I. D., Tully, R. B., Wu, P.-F., et al. 2014, ApJ, 782, 4

Karachentsev, I. D., Makarova, L. N., Tully, R. B., et al. 2018, ApJ, 858, 62

Kashibadze, O. G., & Karachentsev, I. D. 2018, A&A, 609, A11

Kashibadze, O. G., Karachentsev, I. D., & Karachentseva, V. E. 2018, Astrophysical Bulletin, 73, 124

Kashibadze, O. G., Karachentsev, I. D., & Karachentseva, V. E. 2020, A&A, 635, A135

Lee, M. G., Freedman, W. L., & Madore, B. F. 1993, ApJ, 417, 553
Lee, M. G. & Jang, I. S. 2018, Stellar Populations and the Distance Scale (Eds: Joseph Jensen, R. Michael Rich, and Richard de Grijs), ASPCS 514, 143
Lemaître, G. 1933, Annales de la Société Scientifique de Bruxelles, 53, 51
Lynden-Bell, D. 1981, The Observatory, 101, 111
Macaulay, E., Nichol, R. C., Bacon, D., et al. 2019, MNRAS, 486, 2184
Makarov, D., Makarova, L., Rizzi, L., et al. 2006, AJ, 132, 2729
McQuinn, K. B. W., Cannon, J. M., Dolphin, A. E., et al. 2014, ApJ, 785, 3
McQuinn, K. B. W., Skillman, E. D., Dolphin, A. E., et al. 2017, AJ, 154, 51
Méndez, B., Davis, M., Moustakas, J., et al. 2002, AJ, 124, 213
Nasonova, O. G., de Freitas Pacheco, J. A., & Karachentsev, I. D. 2011, A&A, 532, A104
Peirani, S., & de Freitas Pacheco, J. A. 2006, NewA, 11, 325
Peirani, S., & de Freitas Pacheco, J. A. 2008, A&A, 488, 845
Peñarrubia, J., Ma, Y.-Z., Walker, M. G., et al. 2014, MNRAS, 443, 2204
Peñarrubia, J., & Fattahi, A. 2017, MNRAS, 468, 1300
Planck Collaboration, Aghanim, N., Akrami, Y., et al. 2020, A&A, 641, A6. doi:10.1051/0004-6361/201833910
Reid, M. J., Pesce, D. W., & Riess, A. G. 2019, ApJL, 886, L27
Riess, A. G., Macri, L. M., Hoffmann, S. L., et al. 2016, ApJ, 826, 56
Riess, A. G., Casertano, S., Yuan, W., et al. 2019, ApJ, 876, 85
Riess, A. G. 2019, Nature Reviews Physics, 2, 10
Rizzi, L., Tully, R. B., Makarov, D., et al. 2007, ApJ, 661, 815
Sandage, A. 1986, ApJ, 307, 1
Schlafly, E. F., & Finkbeiner, D. P. 2011, ApJ, 737, 103
Schlegel, D. J., Finkbeiner, D. P., & Davis, M. 1998, ApJ, 500, 525
Sirianni, M., Jee, M. J., Benítez, N., et al. 2005, PASP, 117, 1049
Sorce, J. G., Tully, R. B., Courtois, H. M., et al. 2014, MNRAS, 444, 527
Teerikorpi, P., Bottinelli, L., Gouguenheim, L., et al. 1992, A&A, 260, 17
Tikhonov, N. A., & Galazutdinova, O. A. 2020, Astronomy Letters, 45, 750
Tolman, R. C. 1934, Proceedings of the National Academy of Science, 20, 169
Tully, R. B., Shaya, E. J., Karachentsev, I. D., et al. 2008, ApJ, 676, 184
Tully, R. B., Courtois, H. M., Dolphin, A. E., et al. 2013, AJ, 146, 86
Verde, L., Treu, T., & Riess, A. G. 2019, Nature Astronomy, 3, 891
Wong, K. C., Suyu, S. H., Chen, G. C.-F., et al. 2020, MNRAS, 498, 1420